

EVIDENCE FOR QUASI-ISOTROPIC MAGNETIC FIELDS FROM *HINODE* QUIET SUN OBSERVATIONS

A. ASENSIO RAMOS

Instituto de Astrofísica de Canarias, 38205, La Laguna, Tenerife, Spain

Draft version June 5, 2018

ABSTRACT

Some recent investigations of spectropolarimetric observations of the Zeeman effect in the Fe I lines at 630 nm carried out with the *Hinode* solar space telescope have concluded that the strength of the magnetic field vector in the internetwork regions of the quiet Sun is in the hG regime and that its inclination is predominantly horizontal. We critically reconsider the analysis of such observations and carry out a complete Bayesian analysis with the aim of extracting as much information as possible from them, including error bars. We apply the recently developed BAYES-ME code that carries out a complete Bayesian inference for Milne-Eddington atmospheres. The sampling of the posterior distribution function is obtained with a Markov Chain Monte Carlo scheme and the marginal distributions are analyzed in detail. The Kullback-Leibler divergence is used to study the extent to which the observations introduce new information in the inference process resulting in sufficiently constrained parameters. Our analysis clearly shows that only upper limits to the magnetic field strength can be inferred with fields in the kG regime completely discarded. Furthermore, the noise level present in the analyzed *Hinode* observations induces a substantial loss of information for constraining the azimuth of the magnetic field. Concerning the inclination of the field, we demonstrate that some information is available to constrain it for those pixels with the largest polarimetric signal. The results also point out that the field in pixels with small polarimetric signals can be nicely reproduced in terms of a quasi-isotropic distribution.

Subject headings: magnetic fields — Sun: atmosphere — Sun: magnetic fields — line: profiles — polarization

1. INTRODUCTION

Particularly during the last decade, we have witnessed an increasing interest in the investigation of the magnetism of the quiet solar photosphere. There are at least two reasons for this. On the one hand, improvements in the sensitivity of spectro-polarimeters have allowed us to carry out spectropolarimetric observations of great quality in regions of very low magnetic flux. On the other hand, since the quiet Sun covers a fraction larger than 90% of the solar surface, it is important to investigate whether the magnetism of the quiet photosphere plays a significant role on the heating of the outer regions. In case the magnetic energy stored in these apparently non-magnetic zones turns out to be substantial, as claimed by Trujillo Bueno et al. (2004), its impact on the overall energy balance of the solar atmosphere should be accounted for.

The Zeeman polarization signals observed in the quiet Sun are very weak and, even with the best spectropolarimeters, it turns out difficult to detect them and to interpret reliably the observations. One of the main causes for such weak polarization signals is that the filling factor of the magnetic field in the resolution elements of ground based telescopes is very small, of the order of 1% (e.g., Stenflo 1994; Lin 1995; Domínguez Cerdeña et al. 2003; Khomenko et al. 2003; Martínez González et al. 2006a). The reason for this small filling factor may lie in the fact that the field is organized at very small scales and Stokes

V Zeeman signals cancel effectively when averaging fields with several inclinations in the resolution element (linear polarization also cancels when the azimuth is also random). Understanding the probability distribution of field strengths has produced a long debate that is not still resolved (Lin 1995; Lin & Rimmele 1999; Socas-Navarro & Sánchez Almeida 2002; Domínguez Cerdeña et al. 2003; Khomenko et al. 2003; Socas-Navarro et al. 2004; Lites & Socas-Navarro 2004; Martínez González et al. 2006b,a; Domínguez Cerdeña et al. 2006; Orozco Suárez et al. 2007c; Martínez González et al. 2008b; Ramírez Vélez et al. 2008). The reason is that diagnostic tools based on the Zeeman effect suffer from cancellation effects and it is not clear to what extent the probability distribution inferred from the residual Zeeman signals can be compared to the probability distribution of the field strength inside the pixel. Therefore, it is important to develop and apply alternative diagnostic tools that do not suffer from such cancellations. In this respect, we note the efforts of Trujillo Bueno et al. (2004, 2006) applying techniques based on the Hanle effect to infer properties about the magnetic field in the quiet Sun. They concluded that there is a substantial amount of “hidden” magnetic energy in the internetwork regions of the quiet photosphere. Most of these “hidden” fields remain undetected to the Zeeman effect because they are tangled at scales below the resolution of present telescopes or because they are inherently weak. Others have applied Zeeman-based techniques in lines with strong hyperfine perturbations, which make them sensitive to

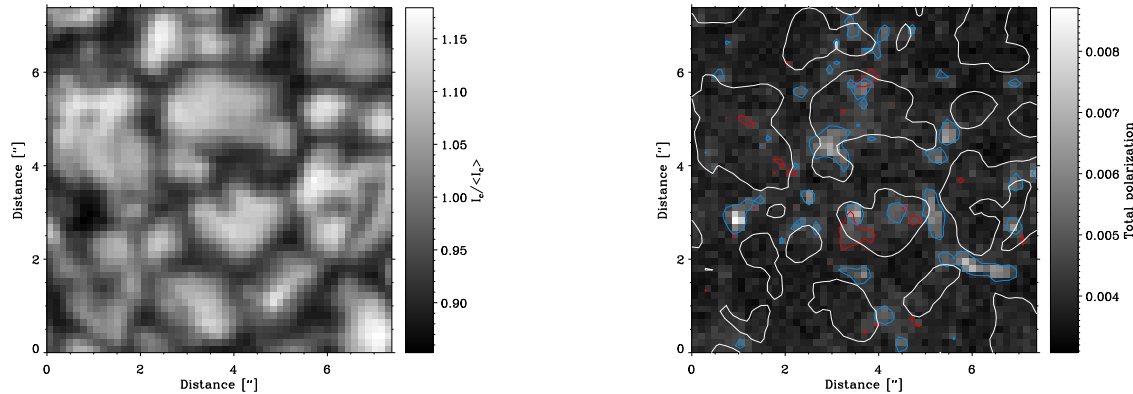


FIG. 1.— The left panel shows the observed intensity (normalized to the average intensity) in the continuum surrounding the 630 nm Fe I doublet. The background image on the right panel presents the total polarization normalized to the average intensity, $\int(Q^2 + U^2 + V^2)^{1/2}d\lambda/\langle I \rangle$. The red and blue contours delineate regions of $\int(Q^2 + U^2)^{1/2}d\lambda/\langle I \rangle > 0.0035$ and $\int(V^2)^{1/2}d\lambda/\langle I \rangle > 0.003$, respectively. The white contours indicate regions where $I_c/\langle I_c \rangle = 1.02$.

the strength of the magnetic field (López Ariste et al. 2002, 2006; Ramírez Vélez & López Ariste 2007; Asensio Ramos et al. 2007a; Ramírez Vélez et al. 2008). The results go in the direction of ubiquitous fields with strengths in the hG regime, which supports the Hanle-effect conclusion of Trujillo Bueno et al. (2004, 2006).

Recent results (Martínez González et al. 2008a) indicate that there is not any apparent variation of the polarimetric properties of the Fe I near-IR doublet at 1.56 μm with the heliocentric angle. This suggests that the magnetism of the quiet Sun remains approximately the same for every observing angle, thus giving weight to the fact that the distribution of magnetic field vectors is quasi-isotropic for the resolutions of ground based telescopes and discards a network-like scenario for the internetwork magnetism. Based on these observations, López Ariste et al. (2007) suggest a scenario in which the observed Zeeman signals are a result of statistical fluctuations of a quasi-isotropic vector field. This scenario suggests a way to reconcile simultaneously the Zeeman and the Hanle results. It also gives an explanation to the reason why the unsigned magnetic flux seems to be the same regardless of the spatial resolution of the observation.

Recent observations carried out with the spectropolarimeter (SP; Lites et al. 2001) aboard *Hinode* (Kosugi et al. 2007) have led to the detection of large amounts of linear polarization signals in the Fe I lines at 630 nm at unprecedented spatial resolutions of $\sim 0.3''$. The interpretation of these signals based on simple inversion methods (Lites et al. 2008) or using more elaborate Milne-Eddington models (Orozco Suárez et al. 2007c; Lites et al. 2008) suggest the presence of magnetic fields with a large horizontal component. The probability distribution of field inclinations given by Orozco Suárez et al. (2007c) suggests that the majority of fields found in the field-of-view are horizontal (with inclinations $\gamma = 90^\circ \pm 15^\circ$), with a certain (small) fraction of fields being almost vertical. It is also necessary to point out that Orozco Suárez et al. (2007a) argued, with the aid of numerical magneto-hydrodynamical simulations, that it is possible to get a good estimation of the magnetic field strength from Milne-Eddington inversions

of *Hinode* data.

If the apparent lack of variation of the polarimetric properties with the heliocentric angle (Martínez González et al. 2008a) and the apparent large presence of horizontal fields at disk center (Orozco Suárez et al. 2007c; Lites et al. 2008) are put together, this would mean that, irrespective of the location in the solar disk, the fields would always be predominantly horizontal. This result indicates that the distribution of magnetic field vectors is indeed close to isotropic since an isotropic vector field distribution always presents a much larger amount of horizontal than vertical field (for all external observers). Therefore, it is of great interest to verify to what extent are the observations (with the presence of noise and the ensuing uncertainties) unambiguously pointing to predominantly horizontal fields.

To this end, we apply BAYES-ME, the Bayesian inference code for Milne-Eddington atmospheres developed by Asensio Ramos et al. (2007b), to a sub-field of the large field-of-view presented by Orozco Suárez et al. (2007c) and Lites et al. (2008) in order to analyze the effect of noise and degeneracies on the retrieved parameters.

2. OBSERVATIONS

The observations are those analyzed by Lites et al. (2008), which were obtained at disk center on 2007 March 10 with the spectropolarimeter aboard *Hinode*. The analyzed map is a small sub-field of $7.4'' \times 7.4''$ taken from a large field-of-view of $302'' \times 162''$. This small sub-field has been also analyzed by Orozco Suárez et al. (2007c) to investigate the properties of very quiet internetwork. The observed spectral region contains the Fe I doublet at 630.1 and 630.2 nm with a resolution close to 3×10^5 . The intensity image in the local continuum normalized to the average continuum intensity in the sub-field is shown on the left panel of Fig. 1 while the total polarization, defined as $\int(Q^2 + U^2 + V^2)^{1/2}d\lambda/\langle I \rangle$, is shown in the right panel of the same figure. This figure also presents the regions of $\int(Q^2 + U^2)^{1/2}d\lambda/\langle I \rangle > 0.0035$ in red contours and $\int(V^2)^{1/2}d\lambda/\langle I \rangle > 0.003$ in blue contours. After calibration, the noise level amounts to $1.2 \times 10^{-3}I_c$ for Stokes V and to $1.1 \times 10^{-3}I_c$ for Stokes Q and U . For more de-

tails on the observations, we refer to Lites et al. (2008).

3. BAYESIAN INVERSION

3.1. BAYES-ME

Although the BAYES-ME code has been extensively described by Asensio Ramos et al. (2007b), we give here a brief overview because of its novel characteristics. The BAYES-ME code is an inversion code built under the framework of the Bayesian approach to inference (see e.g., Neal 1993; Gregory 2005). Let M be a model that is proposed to explain an observed dataset D and let I be a set of sensible *a-priori* information about the problem (for instance, the spectral resolution of the observations). The model M is parameterized in terms of a vector of parameters of length N_{par} , $\boldsymbol{\theta} \in \mathbb{R}^{N_{\text{par}}}$. Due to the presence of noise in the observations, any inversion procedure is not complete by just giving the values of the model parameters that better fit the observations. The full solution to the inference problem is to provide the posterior probability distribution function (pdf) $p(\boldsymbol{\theta}|D, I)$ that describes the probability that a given set of parameters is compatible with the observables given the a-priori knowledge. As a consequence, statistically relevant information about one parameter (irrespective of the value taken by other parameters) can be obtained from this pdf by marginalization (integration) of the rest of parameters. In order to calculate the posterior distribution $p(\boldsymbol{\theta}|D, I)$, the Bayes theorem can be applied to obtain:

$$p(\boldsymbol{\theta}|D, I) = \frac{p(D|\boldsymbol{\theta}, I)p(\boldsymbol{\theta}|I)}{p(D|I)}, \quad (1)$$

where $p(D|I)$ is the so-called *evidence*, a quantity that in the context of parameter estimation is of no importance (since it is a constant that does not depend on the model parameters $\boldsymbol{\theta}$) but that turns out to be crucial in the context of model selection. The distribution $p(\boldsymbol{\theta}|I)$ is denominated the prior distribution and contains all relevant a-priori information about the parameters of the model. Usually, unless some information is available about the value of some parameters, it is common to use uninformative (or vague) priors like bounded uniform distributions or Jeffreys' priors (e.g., Neal 1993). Finally, $p(D|\boldsymbol{\theta}, I)$ is the likelihood, a distribution that characterizes how well a model with parameters $\boldsymbol{\theta}$ reproduces the observed dataset. The Bayes theorem states that the probability that a model M becomes plausible once the information encoded in the data D is taken into account depends on how plausible the model was without data and how well the model fits the data.

Assuming that the observables are represented as a vector $\mathbf{d} \in \mathbb{R}^N$, that the result of evaluating the model M at a given set of parameters $\boldsymbol{\theta}$ is the vector $\mathbf{y} \in \mathbb{R}^N$ and that the observations are contaminated by a noise component characterized by the vector $\mathbf{e} \in \mathbb{R}^N$, we have:

$$d_i = y_i + e_i, \quad \forall i. \quad (2)$$

When the chosen model parameters exactly correspond to those of the observed dataset, the distribution of differences $y_i - d_i$ has to follow the distribution of the noise. Assuming that the noise is Gaussian distributed with a standard deviation given by the vector $\boldsymbol{\sigma} \in \mathbb{R}^N$, the likelihood function is, therefore, given by the following

Gaussian distribution:

$$p(D|\boldsymbol{\theta}, I) \propto \prod_{i=1}^N \exp \left[-\frac{(y_i - d_i)^2}{2\sigma_i^2} \right]. \quad (3)$$

In the case of BAYES-ME, the model M is based on the simplified Milne-Eddington (ME) description of stellar atmospheres. The emergent Stokes profiles are calculated as a linear combination of the emergent Stokes profiles obtained from an arbitrary number of components, each of them characterized by the standard ME parameters. Although the Bayesian approach will allow us in the future to automatically choose the optimal number of components N_c using model selection techniques, N_c is fixed and chosen a-priori in the present version of BAYES-ME (in other words, N_c is part of the a-priori information summarized by I). The vector $\boldsymbol{\theta}$ contains all the ME parameters over which we do inference (the selection of free parameters is completely configurable), while the remaining parameters ME are set as fixed quantities. The BAYES-ME code neglects the fixed parameters and they are not included in the vector $\boldsymbol{\theta}$, although the result is equivalent to the case in which the posterior distribution is marginalized (integrated) over them after setting Dirac delta priors on them (see §3.2). The parameters of the ME atmosphere for each component are: the Doppler width of the line in wavelength units ($\Delta\lambda_{\text{dopp}}$), the line-of-sight component of the macroscopic bulk velocity (v_{LOS}), the gradient of the source function (β), the ratio between the line and continuum absorption coefficients (η_0), a line damping parameter (a) and the magnetic field vector parameterized by its strength, inclination and azimuth with respect to a given reference direction (B , θ_B and χ_B , respectively). We refer, somewhat arbitrarily, to $\Delta\lambda_{\text{dopp}}$, v_{LOS} , β , η_0 and a as the thermodynamical parameters (although their pure thermodynamical character is quite diffuse). Additionally, we take into account the filling factor of each component, f_i , subject to the constraint $\sum_{i=1}^{N_c} f_i = 1$. The maximum number of free parameters is $9N_c - 1$.

In order to sample the posterior distribution function and carry out the ensuing marginalizations, BAYES-ME utilizes a Markov Chain Monte Carlo (MCMC; Metropolis et al. 1953; Neal 1993) scheme based on the Metropolis algorithm. The initial proposal density distribution is a multivariate Gaussian with diagonal covariance matrix that is set to 10% of the allowed range of variation of the parameters. After a configurable initial period, the proposal density is changed to a multivariate Gaussian with a covariance matrix that is estimated from the previous steps of the chain¹. In order to improve convergence, the covariance matrix is multiplied by a quantity that assures that the acceptance rate of proposed models is close to 25%, a value that is the theoretical optimal value for simple problems (Gelman et al. 1996).

3.2. Marginalization

In order to obtain the posterior probability distribution function for one parameter and give estimations and con-

¹ This is an improvement over the version of BAYES-ME presented by Asensio Ramos et al. (2007b) which used a proposal density with diagonal covariance matrix.

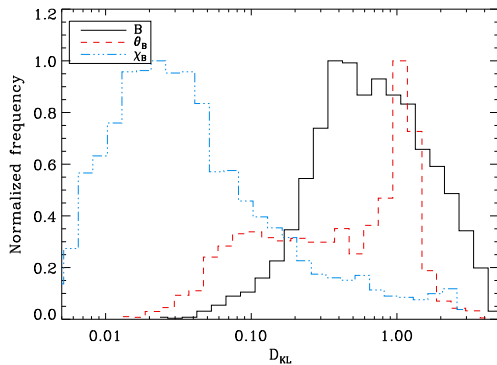


FIG. 2.— Histogram of Kullback-Leibler divergence between the posterior and prior distributions for the magnetic field strength (black line), inclination (red line) and azimuth (blue line). This indicates that the amount of information present in the observations is sufficient to return posterior distributions clearly different from the prior distributions for the magnetic field strength and for the inclination. The information is heavily reduced for the azimuth of the field.

ference intervals, we have to marginalize (integrate out) the rest of parameters:

$$p(\theta_i|D, I) = \int d\theta_1 d\theta_2 \cdots d\theta_{i-1} d\theta_{i+1} \cdots d\theta_{N_{\text{par}}} p(\boldsymbol{\theta}|D, I). \quad (4)$$

Interestingly, the output of any MCMC code is a converged Markov chain for each parameter whose histogram is just proportional to $p(\theta_i|D, I)$. Therefore, calculating marginal posterior distributions is just a matter of making histograms. Any relevant statistical information can be obtained from the distribution or summarized using, in the appropriate cases, the median and confidence intervals or upper/lower limits.

3.3. This analysis

Due to the general character of BAYES-ME, it is possible to adapt it to special inversion schemes like that applied by Orozco Suárez et al. (2007c) for the inversion of *Hinode* quiet-Sun internetwork magnetic fields. We slightly modified BAYES-ME to suit the scheme followed by these authors since our aim is to analyze the reliability of their results. The model used consists of one magnetic Milne-Eddington component contaminated by the presence of a stray-light component. This stray-light contamination, characterized by a filling factor α is obtained locally as the average of the pixels within a box of $1''$ centered in the pixel of interest. The magnetic filling factor (fraction of signal represented by a magnetic atmosphere) is, therefore, $1 - \alpha$. In the analysis, we focus on the magnetic filling factor.

A direct consequence of using a Bayesian inference approach is that we do not need to establish a selection criterion to choose which pixels to invert. For those pixels where the signal-to-noise level is too low, the ensuing posterior probability distributions will straightforwardly show the degeneracies present in the data and the resulting posterior distributions will automatically be very similar to the prior distributions. Therefore, we invert all the pixels in the field-of-view and select afterwards which pixels provide a sufficient amount of information to the inference process. Apart from the pure visual inspection of the resulting marginal probability distributions,

we use a criterium to characterize the pixels in which there is sufficient information. The criterium is based on the calculation of the Kullback-Leibler divergence (KLD; Kullback & Leibler 1951) between the two probability distributions $p(\boldsymbol{\theta}|D, I)$ (posterior distribution) and $p(\boldsymbol{\theta}|I)$ (prior distribution):

$$D_{\text{KL}} = \int_{-\infty}^{\infty} p(\boldsymbol{\theta}|D, I) \log_2 \frac{p(\boldsymbol{\theta}|D, I)}{p(\boldsymbol{\theta}|I)} d\boldsymbol{\theta}. \quad (5)$$

The KLD, always a positive quantity, measures the difference in number of bits between transmitting samples of the distribution $p(\boldsymbol{\theta}|D, I)$ using a code based on $p(\boldsymbol{\theta}|D, I)$ and transmitting samples of the distribution $p(\boldsymbol{\theta}|D, I)$ using a code based on the distribution $p(\boldsymbol{\theta}|I)$. The more different both distributions are, the larger the additional information required. Therefore, larger values of D_{KL} indicate that both distributions are very different. We apply this measure to compare the final posterior probability distribution after the data has been presented to the inference code and the prior distribution. When the data is informative, the posterior distribution is very different from the prior distribution and D_{KL} will be large. Since the priors for the stray-light factor, magnetic field strength, inclination and azimuth of the field are uniform distributions in the intervals $[0, 1]$, $[0, 1500]$ G, $[0^\circ, 180^\circ]$ and $[0^\circ, 180^\circ]$, respectively, the KLD simplifies to:

$$D_{\text{KL}} = \log_2(\theta_{\text{max}} - \theta_{\text{min}}) + \int_{-\infty}^{\infty} p(\boldsymbol{\theta}|D, I) \log_2 p(\boldsymbol{\theta}|D, I) d\boldsymbol{\theta}, \quad (6)$$

where the last term represents the negative of the standard definition of the entropy (sometimes called negentropy) of a continuous probability distribution function. This shows that the limit $D_{\text{KL}} = 0$ is reached when the posterior distribution is equal to the prior distribution and that it can potentially reach very high values for very informative posterior distributions (because the entropy is not bounded from above). According to the results presented below, pixels with $D_{\text{KL}} \gtrsim 0.5$ can be considered to have enough information to roughly constrain a given parameter, although a more conservative threshold would be $D_{\text{KL}} \gtrsim 1$.

4. RESULTS AND DISCUSSION

After applying the BAYES-ME code to all the pixels in the field-of-view, the results consist of converged Markov chains for each parameter. As an additional test for convergence, we rerun the code several times obtaining almost indistinguishable results. By making histograms of each chain, we obtain the posterior distribution function marginalized over all parameters except the one of interest. These marginal posterior distribution functions show how the information encoded on the observed Stokes parameters constrain every individual parameter. In principle, the correct answer to the inversion process would be to give such posterior distributions for each parameter and each pixel. Since this is obviously not feasible for presentation purposes, we follow a different approach and try to condense the important statistical information present in each chain. We focus only on the properties of the magnetic field vector thanks to the results of Westendorp Plaza et al. (1998), who demonstrated that the cross-talk between

thermodynamical and magnetic parameters is of reduced importance in Milne-Eddington inversions. The reason for this behavior has to be found on the large difference between the response functions for the Milne-Eddington thermodynamical and magnetic parameters, as elegantly shown by Orozco Suárez & Del Toro Iniesta (2007). Note that, due to the Bayesian approach that we follow, the marginal posterior distributions for the magnetic field parameters automatically include information about all possible values of these thermodynamical parameters weighted by their probability.

4.1. Amount of information

The first key point is to estimate how much information about every parameter can be inferred from the observables. To this end, we analyze the Kullback-Leibler divergences. Figure 2 shows the histogram of D_{KL} for the marginal posterior distributions of the magnetic field strength, inclination and azimuth in all pixels. It is clear from this figure that the amount of information available to constrain the azimuth is very poor because D_{KL} is very close to zero for all the pixels. This is a consequence of the fact that almost all pixels present posterior distributions for the azimuth that are indistinguishable from the uniform prior distribution, as we demonstrate below. There is more information available for constraining the field strength and inclination (larger values of D_{KL}) although several pixels present posterior distributions that are still similar to the prior. Table 1 summarizes the percentage of pixels with relevant information for each parameter in the field-of-view.

Of interest is also the analysis of the horizontal variation of D_{KL} shown in Fig. 3. The results clearly indicate what has been summarized in Fig. 2. For clarity, we have also indicated with contours the regions where $I_c/I_c = 1.02$, which may serve as a rough indication of the position of the brighter parts of granules. Several interesting points can be inferred from these plots.

First, a large amount of pixels present large values of $D_{\text{KL}}(1 - \alpha)$ (bright points in the upper left panel of the figure). These pixels have, as we show later in Fig. 4, posterior distributions for the magnetic filling factor with a very conspicuous peak close to zero. They correspond to pixels in which the polarization signal is extremely low and well below the noise. In such a situation, and since the intensity profile is non-zero, the best fit is accomplished with $\sim 100\%$ stray-light contamination. For this reason, the very same white pixels for the $D_{\text{KL}}(1 - \alpha)$ map are typically dark in the $D_{\text{KL}}(B)$ map because the noise rapidly destroys the information needed to give a reliable value of the magnetic field strength. It is important to point out that these results are only valid for the present noise level of the observations and that results would surely change if a better signal-to-noise ratio had been achieved.

Second, it is obvious from the middle panels of Fig. 3 that there is less information to constrain the inclination and azimuth of the field (especially for the azimuth). However, it is interesting to point out that there is apparently more information available in intergranular lanes than in granules, in many cases corresponding to pixels with the largest polarization signals. These polarization signals in the intergranular lanes are mainly circular polarization, as shown in Fig. 1. It is also obvious from Fig.

TABLE 1
PIXELS WITH KULLBACK-LEIBLER DIVERGENCES ABOVE DIFFERENT THRESHOLDS.

Parameter	$N(D_{\text{KL}}) > 0.5$	$N(D_{\text{KL}}) > 1$	$N(D_{\text{KL}}) > 2.5$
α	100.0%	100.0%	77.5%
B	64.8%	36.9%	9.2 %
θ_B	49.8%	33.7%	1.5%
χ_B	7.0%	3.8%	0.8%
B_{\parallel}	90.6%	61.0%	14.1%
ϕ	100.0%	100.0%	99.7%

3 the appearance of patches in the field-of-view where the field strength, inclination and azimuth can be nicely constrained. Note that, according to Fig. 1, they correspond to patches where the linear polarization signal is large. This demonstrates, as we shown in §5 and Fig. 8, the well-known fact that a linear polarization signal well above the noise level produces a well constrained inferred magnetic field vector. Particularly frustrating is the fact that, at this noise level and apart from these patches, the information for constraining the azimuth of the field is almost negligible.

Finally, the lower panels present the horizontal variation of the Kullback-Leibler divergence for B_{\parallel} , the longitudinal component of the magnetic field vector (lower left panel) and $\phi = (1 - \alpha)B_{\parallel}$, the longitudinal magnetic flux density (lower right panel). The information available for the line-of-sight component of the magnetic field vector is very similar to that of the field itself but slightly larger because it is augmented with the knowledge of the inclination angle. On the contrary, the longitudinal magnetic flux density shows a very clear correlation with the granulation pattern. All values of $D_{\text{KL}}(\phi)$ are clearly larger than 1, showing that there is sufficient information in all the pixels to obtain information about this quantity, which clearly changes smoothly from pixel to pixel.

4.2. Marginal posteriors

In order to understand the typical values of D_{KL} for which we can consider that the posterior distribution is clearly different from the prior distribution, we show in Fig. 4 examples of the posterior distributions for the magnetic filling factor, magnetic field strength, inclination and azimuth for different values of D_{KL} . We also present the posterior distributions for the longitudinal component of the field and for the longitudinal magnetic flux density. They show, in general, that nicely constrained parameters present $D_{\text{KL}} \gtrsim 1$. In order to facilitate the comparison, we also overplot the prior distribution in dashed lines.

As already discussed, the stray-light contamination is usually well constrained, at least for values of $D_{\text{KL}}(1 - \alpha) \geq 1.3$ (see upper left panel of Fig. 4). Smaller values present posterior distributions that can be considered commensurate with the prior distribution. Intermediate values typically correspond to those points in which the stray-light contamination amounts to $\alpha \sim 0.8$ on average, while the Bayesian results for those points with large values of $D_{\text{KL}}(1 - \alpha)$ point to an almost non-magnetic atmosphere. As already discussed by Orozco Suárez et al. (2007b), this behavior is a consequence of the fact that the stray-light contamination is mainly sensitive to the Stokes I profile and can be constrained fairly well irrespective of the noise level in the rest of Stokes param-

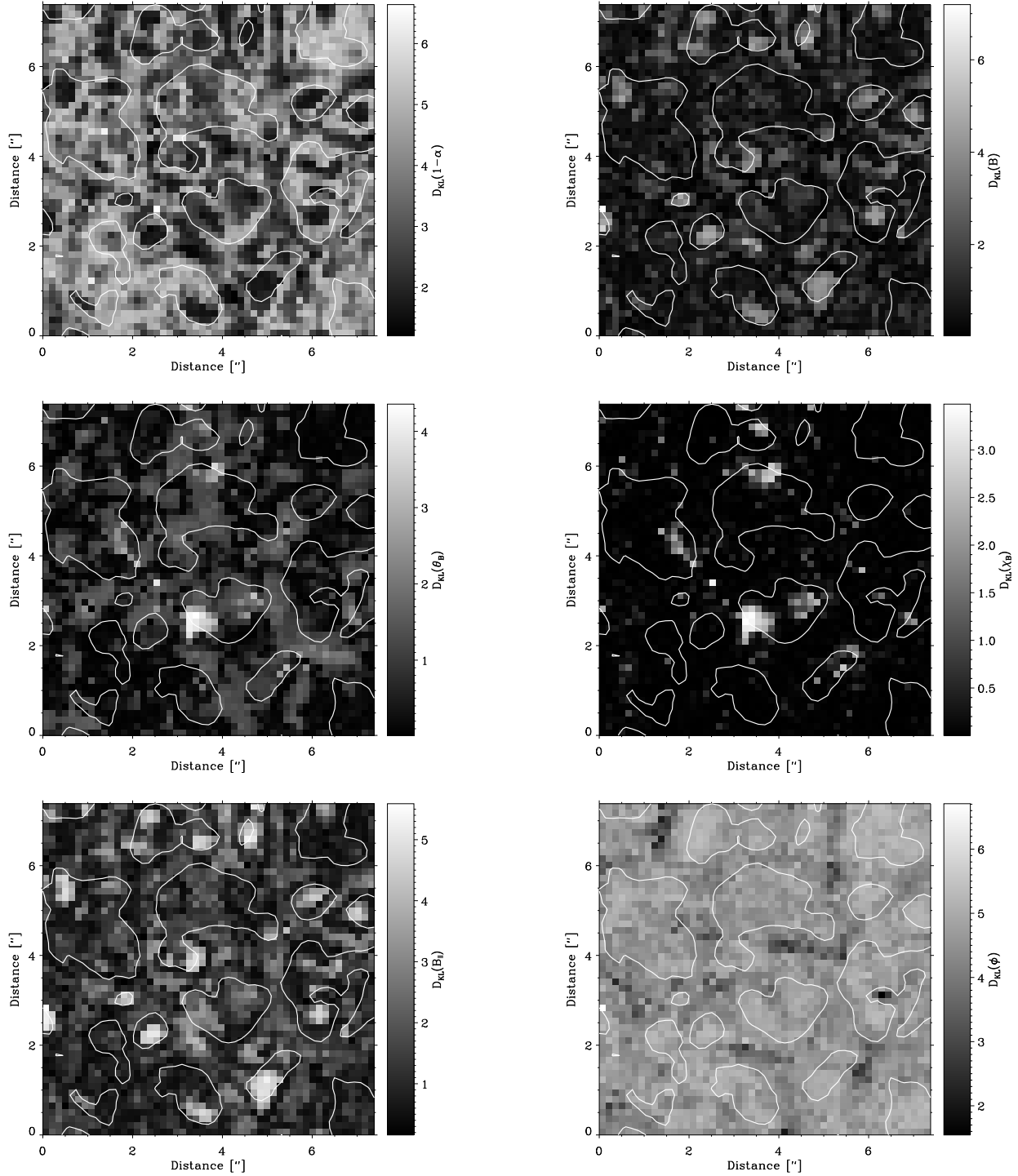


FIG. 3.— Horizontal variation of the Kullback-Leibler divergence between the posterior and prior distributions for the magnetic filling factor (upper left panel), the magnetic field strength (upper right panel), field inclination (middle left panel), field azimuth (middle right panel), longitudinal component of the field (lower left panel) and longitudinal magnetic flux density (lower right panel). The contours indicate regions where $I_c / \langle I_c \rangle = 1.02$.

ters.

A similar behavior is seen in the marginal posteriors for the magnetic field strength (upper right panel of Fig. 4), although the results are clearly less informative. When $D_{\text{KL}}(B) \lesssim 0.1$, we can state that the posterior distribution is very similar to the prior distribution (marked as a horizontal dashed line), so that these pixels do not contain enough information for constraining this parameter. When $D_{\text{KL}}(B)$ increases, the posterior distribution functions usually show the same behavior, peaking at magnetic fields close to zero but with an extended tail towards higher values. For such distributions with extended tails, the only quantity with statistical meaning that we can give to summarize the results is an upper limit (with 68% or 95% confidence). Although an analysis of these upper limits will be presented in §4.3, it is possible to see from the upper right panel of Fig. 4 that they are systematically favouring hG fields with respect to stronger fields. The set of points associated to the bright patch of the middle panels of Fig. 3 produce marginal posterior distributions with a Gaussian-like shape peaking in the 400-600 G range but with tails that completely discard fields in the kG regime. This represents one of the key conclusions of our work.

After the claims raised by Lites et al. (2008) and Orozco Suárez et al. (2007c) about the large amount of very inclined magnetic fields (with a distribution that peaks near 90°), it is interesting to analyze how much information is still encoded in the Stokes profiles of the *Hinode* observations under study as analyzed with the suggested Milne-Eddington model. It is important to point out that, although the presence of a large amount of inclined fields was inferred by Lites et al. (2008) and Orozco Suárez et al. (2007c) with data with the same noise level as those presented here, it was also confirmed by Lites et al. (2008) with observations with a noise level a factor ~ 4 smaller. The middle left panel of Fig. 4 shows the marginal posterior probability distribution functions for the field inclination. We have verified that it is fundamental to have $D_{\text{KL}}(\theta_B) \geq 0.5$ in order to end up with a posterior distribution function clearly different from the prior distribution (dashed line). According to Table 1 and Fig. 2, the number of points fulfilling this condition is close to 50%. We have to point out that many of these points present posterior marginal distributions similar to the green or blue curves in the middle left panel of Fig. 4. Such posteriors, that discard half of the range of inclinations but give equal probability to the other half, are a consequence of the small Stokes V signal that is still enough to univoquely select the direction of the field but not its inclination. In other words, the polarity of the field is easily recovered but it remains impossible to constrain more the inclination. This means that, even for pixels with low signals (well below the threshold), there is enough information to, at least, detect the polarity of the field. Obviously, when the filling fraction of the magnetic component is very small and the magnetic field is in the weak field regime, the field cannot be recovered uniquely. This translates into posterior distribution functions with long tails for the field strength and the field inclination, as a consequence of the marginalization over the rest of variables (see Asensio Ramos et al. 2007b).

Concerning the field azimuth (middle right panel of

Fig. 4), the results are not very encouraging. The majority of marginal posterior distributions commensurate with the prior distribution. Only in approximately 1% of the field-of-view we find marginal posteriors with a clear peak favoring a certain subset of azimuths (those corresponding to the white patches of the middle right panel of Fig. 3), while in $\sim 4\%$ of the points, the information encoded in the Stokes profiles allows to roughly determine the azimuth but with a very large error bar.

The lower two panels of Fig. 4 present several posterior distributions for B_{\parallel} and ϕ for pixels with different values of the Kullback-Leibler divergence. The dashed lines show the prior distributions, whose functional forms are, assuming uniform priors for α , B and θ_B :

$$p(B_{\parallel}) = \frac{1}{1500\pi} \left\{ -\ln |B_{\parallel}| + \ln \left[1500 + \sqrt{1500^2 - B_{\parallel}^2} \right] \right\}, \quad (7)$$

for the longitudinal component of the field, and

$$p(\phi) = \frac{1}{1500\pi} \int_{|\phi|}^{1500} \frac{2 \ln 2 + \ln 3 + 3 \ln 5 - \ln x}{\sqrt{x^2 - \phi^2}} dx, \quad (8)$$

for the longitudinal magnetic flux density. Note that $p(B_{\parallel} = 0)$ and $p(\phi = 0)$ tend to infinity in this case although the distribution has finite area. We believe it is important to point out that the product of random variables distributed uniformly can result in highly non-trivial distributions. Consequently, *it is extremely important to understand which is the inherent prior information introduced in any inversion method because, when the data is non-informative, the parameters recovered can be strongly influenced by the prior.*

The posterior distributions for B_{\parallel} for small values of $D_{\text{KL}}(B_{\parallel})$ resemble the prior distribution. They become much more distinct when enough information is encoded in the Stokes profiles, thus resulting in peaked posterior distributions without extended tails. Interestingly, as a consequence of the multiplication by the well-determined magnetic filling factor, all the posterior distributions for the longitudinal flux density are quite dissimilar to the prior, except perhaps those points with small values of the Kullback-Leibler divergence, i.e., $D_{\text{KL}}(\phi) \approx 1.7$.

4.3. Parameter estimation

According to the results of the previous section, the magnetic filling factor and the upper limit of the magnetic field strength can be nicely inferred for a relatively large amount of pixels. Likewise, it is possible to set constraints on the field inclination for a subset of the field-of-view, while almost no pixels contain information about the field azimuth. Since the posterior distributions for $1 - \alpha$ are fairly peaked, we summarize them using the median value, together with the upper 95% confidence limits. It is calculated as the value that encloses 95% of the total area of the posterior distribution starting from $1 - \alpha = 0$. The results are shown in the upper left panel of Fig. 5, where we plot the histogram of median values in black and the histogram of the 2σ limit in red, respectively. The vertical dashed line indicates the position of the most abundant value found by Orozco Suárez et al. (2007c). Note that if the plot is done in linear scale almost all the points collapse to $1 - \alpha \approx 0$. Concerning the confidence intervals, the histograms indicate that

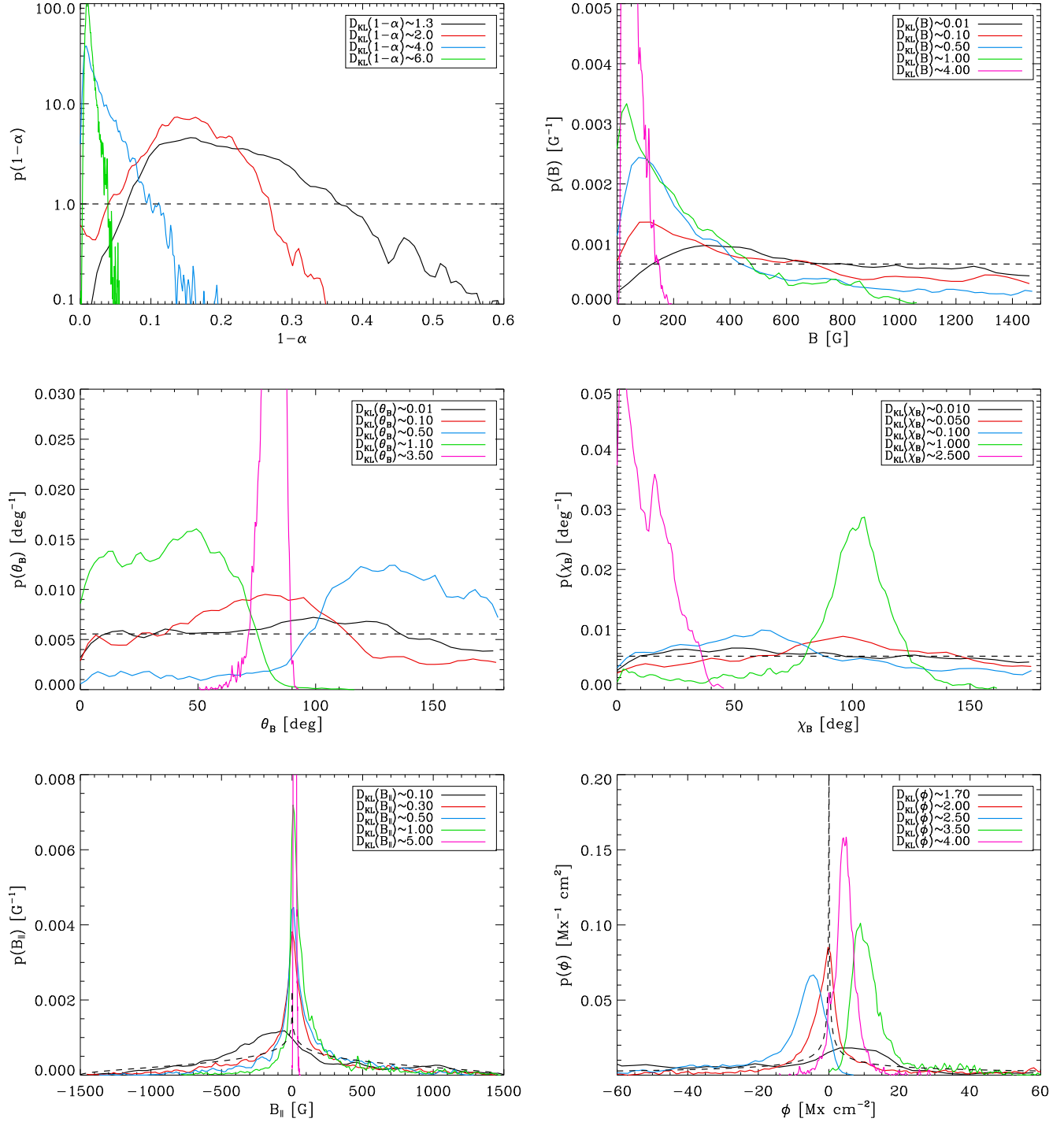


FIG. 4.— Marginal posterior distribution functions for the magnetic filling factor (upper left panel), magnetic field strength (upper right panel), field inclination (middle left panel), field azimuth (middle right panel), longitudinal component of the field vector (lower left panel) and longitudinal magnetic flux density (lower right panel) for several pixels with different values of the Kullback-Leibler divergence. The selected pixels are representative of zones where there is no information about the parameters (small values of D_{KL}) and those in which the information is enough to restrict to some extent their values (large values of D_{KL}). The posterior distributions have been smoothed with a Gaussian kernel for aesthetic purposes. For comparison, the prior distribution is shown in dashed lines.

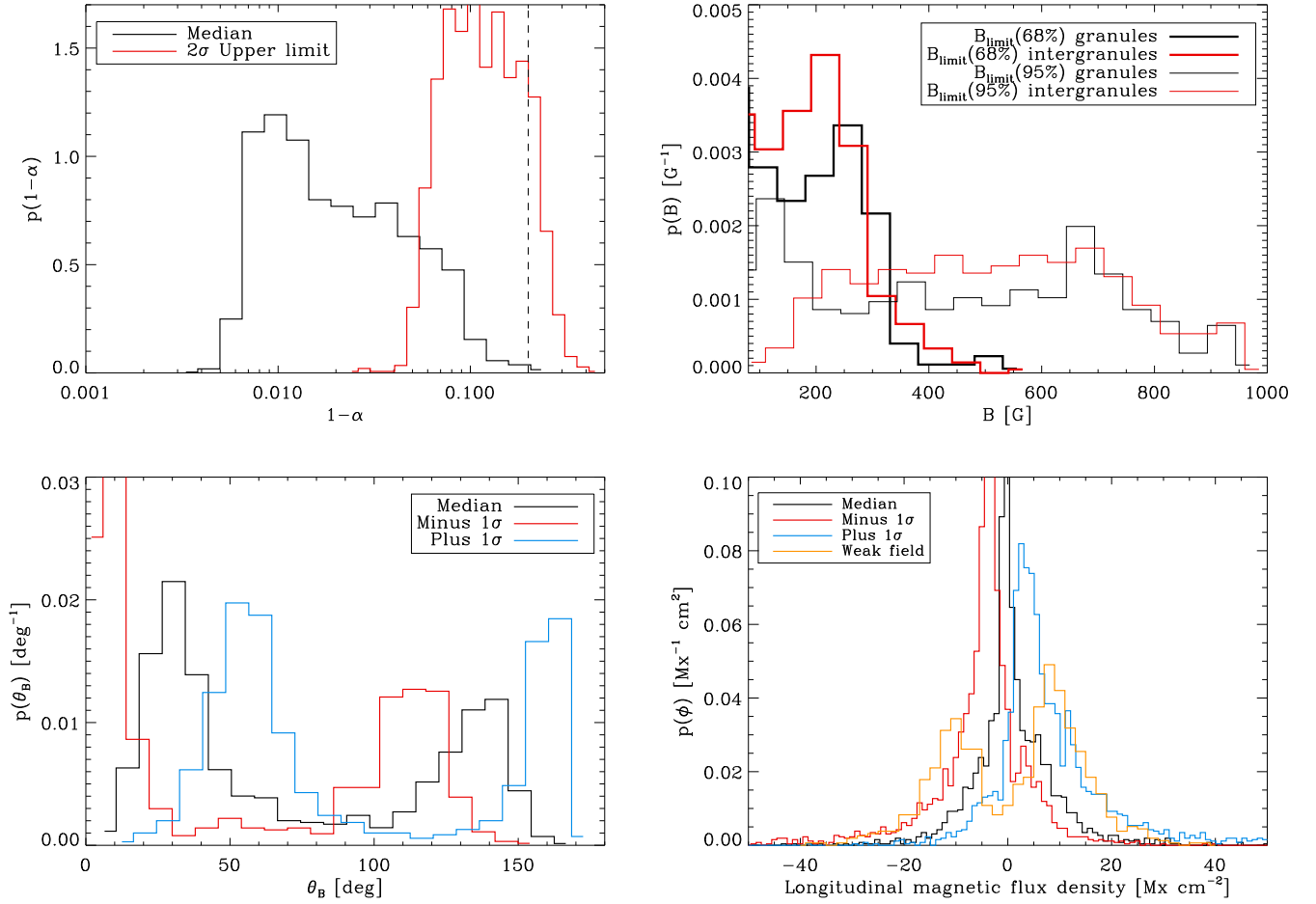


FIG. 5.— Histograms showing the parameters estimated from the marginal posterior distribution functions for the magnetic filling factor (upper left panel), upper limit of the magnetic field strength (upper right panel) and inclination (lower left panel) and longitudinal magnetic flux density (lower right panel) for those pixels containing enough information. Note that this include 100% of the pixels for $1 - \alpha$ and ϕ , 36.9% of the pixels for B and only 33.7% of the points for θ_B . For the magnetic field strength, the results have been separated into granules and intergranules.

they are relatively narrow, completely discarding magnetic filling factors with $1 - \alpha > 0.4$ at 95% confidence. This upper limit is in rough agreement with the results presented by Orozco Suárez et al. (2007c).

Because the shape of the posterior distributions for the magnetic field strength only allows us to put upper limits in this parameter, we show in the upper right panel of Fig. 5 the histograms of the horizontal variation of the 68% and 95% upper limits of the distributions only for those pixels having $D_{\text{KL}}(B) > 1$ (roughly one third of the field-of-view, according to the results shown in Table 1). For illustration, we have also divided the field-of-view into pixels belonging to granules and to intergranular lanes. The selection criterion we have used is very simplistic and it is based on selecting pixels with $I_c/\langle I_c \rangle > 1.02$ as granules and pixels with $I_c/\langle I_c \rangle < 0.98$ as intergranules. The histograms indicate a quite unclear difference between the limit field in “granules” and “intergranules”, with the histogram of the 68% confidence limit field around 200 G for both cases. The histograms are obviously shifted towards higher field strengths for the 95% confidence histograms but the results undeniably discard fields above ~ 900 G. According to the information available in the Stokes profiles observed with *Hinode*, these histograms are the only statistically relevant result that one can give about the magnetic field strength, except for some individual points where the posterior distribution presents a clear Gaussian-like shape. It is important to note that these results do not discard probability distribution functions peaking at much smaller fields like those present in MHD simulations (Vögler et al. 2005), or those inferred from infrared data (e.g., Lin 1995; Khomenko et al. 2003; Martínez González et al. 2006b; Martínez González et al. 2008b) or lines with hyperfine structure (Ramírez Vélez et al. 2008). However, they discard pixels in the field-of-view having fields above 900 G. In this sense, the results obtained by Orozco Suárez et al. (2007c) using standard Levenberg-Marquardt inversion schemes are inside the limits posed by our Bayesian analysis.

Only around 50% of the Stokes profiles observed in the field-of-view contain enough information for introducing constraints on the inclination ($D_{\text{KL}}(\theta_B) > 0.5$). If we summarize the inferred inclination by the median value of the posterior distribution (without taking into account its spread), the result is shown in the lower left panel of Fig. 5. Because of the typically extended shape of the posterior distributions for the field inclination, the results are therefore of reduced interest as representative of the statistical properties of the magnetic field inclination in the whole field-of-view. The histograms of 68% confidence intervals are also presented. The results indicate that the median values peak close to 30° and 140° with a dispersion around these values. This is a consequence of the fact that for many points we can only distinguish the polarity of the field (with the posterior distribution resembling, for instance, the curve for $D_{\text{KL}}(\theta_B) = 1.1$ in the middle left panel of Fig. 4) and the median value is close to the center of the $[0^\circ, 90^\circ]$ or $[90^\circ, 180^\circ]$ intervals.

Finally, the lower right panel of Fig. 5 represents the median (in black line) and the $\pm 1\sigma$ values (red and blue lines) of the magnetic flux density as obtained from the marginal posterior distributions of the lower right panel of Fig. 4. For comparison, we also show the histogram

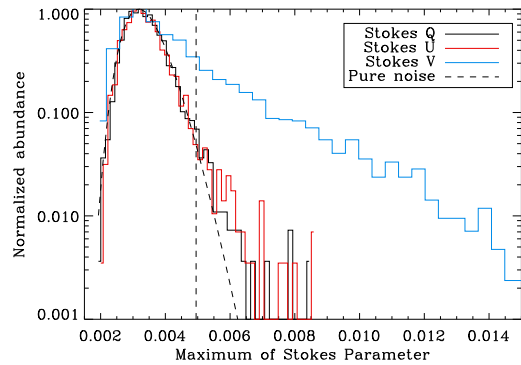


FIG. 6.— This figure shows the histogram of maximum amplitudes of Stokes Q , U and V . The histogram in dashed line is the corresponding to pure noise calculated using order statistics. The vertical dashed line indicates the threshold of 4.5 times the noise level.

of the magnetic flux density obtained under the assumption of the weak field regime for those pixels with signals above 4.5 times the noise level. The magnetic flux density histogram estimated under the assumption of weak field regime lies inside the Bayesian $\pm 1\sigma$ confidence region. This is a consequence of the fact that, even if the cross-talk between the strength and inclination of the magnetic field vector and the magnetic filling factor cannot be disentangled, the product $\phi = (1 - \alpha)B \cos \theta_B$ can be estimated with confidence.

4.4. Available information

The fundamental point to clarify at the light of the results shown in the previous sections is which is the mechanism (or combination of mechanisms) that is destroying the information about the magnetic field vector in the observed Stokes profiles. To this end, we first analyze the fraction of pixels with signal above the noise level. Figure 6 shows the histogram of the maximum amplitude of Stokes Q , U and V in each pixel (the quantity chosen by Orozco Suárez et al. 2007c, to set their threshold). The histogram in dashed line presents what one would obtain for a pure noisy case with the same standard deviation of the *Hinode* data, while the vertical dashed line indicates the threshold of 4.5 times the noise level. Note

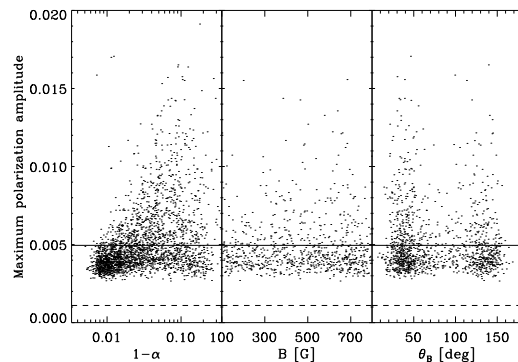


FIG. 7.— Inferred magnetic filling factor, the upper limit of the field and the inclination of the field versus the maximum amplitude of the polarization profiles, i.e., $\max\{Q(\lambda)/I_c, U(\lambda)/I_c, V(\lambda)/I_c\}$. The dashed horizontal line shows the noise level and the solid line presents the threshold of 4.5 times the noise level. This shows that pixels with amplitudes below and above the threshold of 4.5 times the noise level present similar behaviors.

that the probability distribution function of a random variable that results from taking the maximum of a finite number of normal random quantities (the pixels in the wavelength direction of the camera) can be obtained using techniques of order statistics (David 1981). For the case of Gaussian noise and 90 points in wavelength direction, this gives the skewed distribution shown in Fig. 6. We have empirically verified that the distribution peaks at $\sim 2.5\sigma$, where σ is the standard deviation of the noise.

It is clear that Stokes Q and U profiles are mainly dominated by noise in a large fraction of the pixels, with a tail towards large amplitudes that is slightly heavier than for the case of pure Gaussian noise. The threshold chosen by Orozco Suárez et al. (2007c) appropriately isolates these points. On the contrary, the Stokes V amplitudes are not dominated by noise for amplitudes above the threshold. This means that, in the majority of the pixels, only the (possibly modified) information encoded in Stokes I and Stokes V remains. Note that the inference is carried out using the full wavelength variation of the profile, so that it is certain that, even if the amplitude is close to the noise level, some information may still remain in the correlation between different wavelength points along the profile. When the stray-light contamination is large in the pixels, the information present in Stokes V is also efficiently masked by the noise because the circular polarization signal decreases. Consequently, once the stray-light contamination is set by adapting the model until fitting Stokes I , the upper limit in the field strength is essentially set by the remaining amplitude of Stokes V .

The fact that noise is not the only contributor to the lack of information in the Stokes profiles can be reinforced thanks to the results presented in Fig. 7. In this figure we plot the median values of the magnetic filling factor, the 68% upper limit of the magnetic field strength and the median value of the inclination of the field for those pixels in which $D_{\text{KL}}(1 - \alpha) > 1$, $D_{\text{KL}}(B) > 1$ and $D_{\text{KL}}(\theta_B) > 0.5$ versus the value of $\max\{Q(\lambda)/I_c, U(\lambda)/I_c, V(\lambda)/I_c\}$. We also show the noise level as a horizontal dashed line and 4.5 times the noise level as a horizontal solid line. All pixels present significant signal of Stokes Q , U or V , with this signal always above $\sim 2\sigma$. Except for the stray-light contamination, the points above and below the threshold set by Orozco Suárez et al. (2007c) present roughly similar results and seem to be independent of the amplitude of the profiles. A different behavior is found for the stray-light contamination. Profiles with signals below the threshold show systematically very large stray-light contaminations (with $1 - \alpha \sim 0.01$), while pixels above the threshold show systematically smaller contaminations.

Although apparently obvious, another quantitative conclusion that we can extract from our analysis is that one needs to detect signal in Stokes Q and U in order to get a good estimation of the inclination. This is demonstrated in the right panel of Fig. 8. We present the posterior distribution function for two pixels with negligible Stokes Q and U that are not detected above the noise level (red curves). The posterior distributions agree with the prior uniform distribution, so no information about the inclination is available. On the contrary, for the two pixels for which the Stokes Q and U signal are well above the noise level the posterior distribution func-

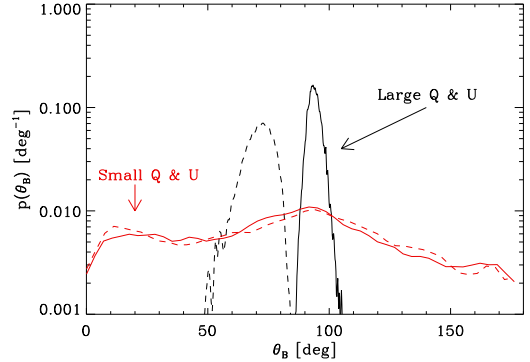


FIG. 8.— Posterior distributions for the field inclination in two pixels with sizable Stokes Q and U signals (black solid and dashed lines) and in two pixels with negligible Stokes Q and U signals (red solid and dashed lines).

tions are clearly different from the prior distribution.

5. QUASI-ISOTROPY OF THE MAGNETIC FIELD

An obvious question that arises after our analysis is whether it is possible to extract some solid conclusions about the field inclination from the information available in the observations. In order to answer to this question, we have calculated, for each pixel, the following quantities, that give the fraction of the total area of the posterior distribution function that is enclosed in a given interval:

$$f(\theta_1, \theta_2) = \int_{\theta_1}^{\theta_2} p(\theta_B) d\theta_B, \quad g(\chi_1, \chi_2) = \int_{\chi_1}^{\chi_2} p(\chi_B) d\chi_B. \quad (9)$$

The posterior marginal distributions $p(\theta_B)$ and $p(\chi_B)$ are normalized to unit area. The quantity f represents the probability that the inclination of the field lies between θ_1 and θ_2 . In an isotropic field, one finds the same amount of vectors whose inclination lies between 0° and 60° (or between 120° and 180°) than between 60° and 90° (or between 90° and 120°). In other words, using Eq. (9), $f(|\mu| < 0.5) = f(|\mu| \geq 0.5) = 1/2$, with $\mu = \cos \theta_B$. Correspondingly, the quantity g represents the probability that the azimuth of the field lies between χ_1 and χ_2 . In an isotropic field, one finds the same amount of vectors with azimuths between 0° and 45° than between 45° and 90° (the same happens for azimuths between 90° and 180°). According to our imposed prior on the azimuth, we are not able to distinguish a purely random azimuth from a situation in which we have a non-constrained azimuth. The left panel of figure 9 shows the histogram of the quantity $f(|\mu| < 0.5)$ for those points whose polarimetric signal is above the threshold (dashed line) and below the threshold (solid line). Note that, in an isotropic field, the histogram of $f(|\mu| < 0.5)$ should peak at $1/2$ (with some natural dispersion). Although the histogram of pixels with signals below the threshold (dashed line) clearly point towards a quasi-isotropic distribution, the histogram of pixels with signals above the threshold (solid line) indicates a clearly non-isotropic distribution. In this last case, the histogram of high-inclination fields (fields with $|\mu| < 0.5$) peak at values conspicuously smaller than $1/2$. For completeness, the histogram for low-inclination fields (fields with $|\mu| \geq 0.5$) peaks therefore at values larger than $1/2$. Note that,

according to our imposed prior (uniform in θ_B), in the complete absence of information on the Stokes profiles, $f(|\mu| < 0.5)$ should converge to the value 1/3. The fact that the histogram peaks close to 1/2 means that information about the quasi-isotropicity of the magnetic field vector is still available. Concerning the azimuth, we plot in the right panel of Fig. 9 the histogram of the pixel-to-pixel variation of the posterior mass for the azimuth between 45° and 135° . According to the previous discussion, this should be close to 1/2 for an isotropic field, although this should also be the case for completely non-constrained azimuths. We find that this is the case in general for all points in the field-of-view, irrespective of the amplitude of the polarimetric signal, thus suggesting the idea that the azimuth of the field is not clearly organized. Therefore, for pixels with polarimetric signal below 4.5 times the noise level, the field is apparently quasi-isotropic (as a vector field). We point out that this result is in agreement with the quasi-isotropic character of the field found by Martínez González et al. (2008a). A more deep analysis of improved data is mandatory to evaluate this property of the field.

6. COMPARISON WITH χ^2 -MINIMIZATION

The model we propose for explaining the observations is exactly that used by Orozco Suárez et al. (2007c). Since we are using uniform priors for all the variables and we are sampling the full posterior distribution, we are also capable of recovering their results by just looking at the combination of parameters that gives the maximum value of $p(\theta|D, I)$. Such model is also the global minimum of the χ^2 merit function and should be equivalent to that found by Orozco Suárez et al. (2007c) using Levenberg-Marquardt techniques if the method was successful in locating the global minimum. We point out that the maximum-a-posterior (MAP) model, although it represents the model that better fits the observations, is statistically equivalent to all those models inside the 68% confidence region, as stated above. Consequently, the presence of noise induces that the MAP model cannot be preferred over the rest of compatible models based on statistical justifications.

The correct Bayesian way of giving constraints for individual parameters is done after marginalizing the rest of parameters (which are accounted for with their associated probabilities). Unless the multidimensional posterior distribution is peaked (Gaussian-like, for instance), the MAP model and the marginal value for each parameter do not coincide. This is especially relevant when parameters are highly degenerate, which is the case with this dataset. We have verified that the MAP results agree well with those presented in Fig. 2 of Orozco Suárez et al. (2007c), as shown in Fig. 10, but they usually differ from the value at the peak of the marginal distribution. This is a clear indication of the presence of strong degeneracies. All points whose polarimetric signal is not above 4.5 times the noise level are set to black in Fig. 10. The histogram of MAP field inclinations presents a shape very similar to that found in the lower left panel of Fig. 5, with two peaks symmetrically placed around 90° . Interestingly, the MAP estimation of the field inclination for those pixels with amplitude signals below the threshold tends to be very close to 90° . Indeed, these pixels also correspond to the points with

$D_{KL}(\theta_B) < 0.5$. This suggests that many of the points giving $\theta_B \sim 90^\circ$ in Orozco Suárez et al. (2007c) should be reconsidered within a Bayesian framework in order to investigate whether this value is really representative or they are just a subproduct of the lack of information on the Stokes profiles. The fact that many of these points with inclination angles of the magnetic field close to 90° are located inside regions with low polarization amplitudes and/or surrounding regions of large signal (see Fig. 1 of Orozco Suárez et al. 2007c) points towards the second possibility. This analysis is left for the future.

7. CONCLUSIONS

We have applied the BAYES-ME inference code to *Hinode* spectropolarimetric observations of the internet-work quiet Sun. The deep analysis carried out under the Bayesian inference approach and using a simplified Milne-Eddington model of one magnetic component with a stray-light contamination leads us to conclude that there is information in the observables to put upper limits to the magnetic field strength and to give a good estimation of the stray-light contamination. The results indicate that the magnetic field strength is clearly in the hG regime with 95% confidence, so that fields in the kG regime are effectively discarded. All the results presented in this paper depend on the assumption that the model proposed explains the observables. It might be the case that a simpler or more complex model allows us to extract more information from the observables because it inherently reduces some of the degeneracies. This is an issue left for future investigation.

Concerning the field inclination, the information present in the *Hinode* Stokes profiles used by Lites et al. (2008) and Orozco Suárez et al. (2007c) is clearly not enough to tightly constrain it. However, since after the Bayesian analysis we have in hands the full posterior distribution for each parameter and each pixel, we have been able to conclude that the amount of high-inclination fields (with $\theta_B < 60^\circ$ and $\theta_B > 120^\circ$) and low-inclination fields (with $60^\circ < \theta_B < 120^\circ$) is essentially the same for pixels with polarimetric amplitudes below 4.5 times the noise level. This suggests that the magnetic fields of part of the quiet solar photosphere are well described by an quasi-isotropic distribution. This supports the results of Martínez González et al. (2008a). For those pixels with polarimetric amplitudes above the threshold, the inclinations are clearly constrained.

This paper also demonstrates that, although BAYES-ME² is computationally more intensive than standard Levenberg-Marquardt codes, it is feasible to analyze real data under the Bayesian framework. The analysis of the ~ 2500 pixels of the map was done in less than 8 hours in a standard desktop computer, at a rate of ~ 10 seconds per pixel. In spite of the increase in computing time, the amount of information inferred from the analysis is far more complete than that from standard gradient descent inversions. This has allowed us to verify which parameters are constrained by the observations and permits the user to yield conclusions based purely on the observations, clearly showing when conclusions can be flawed by a-priori assumptions.

² BAYES-ME is freely available from the author.

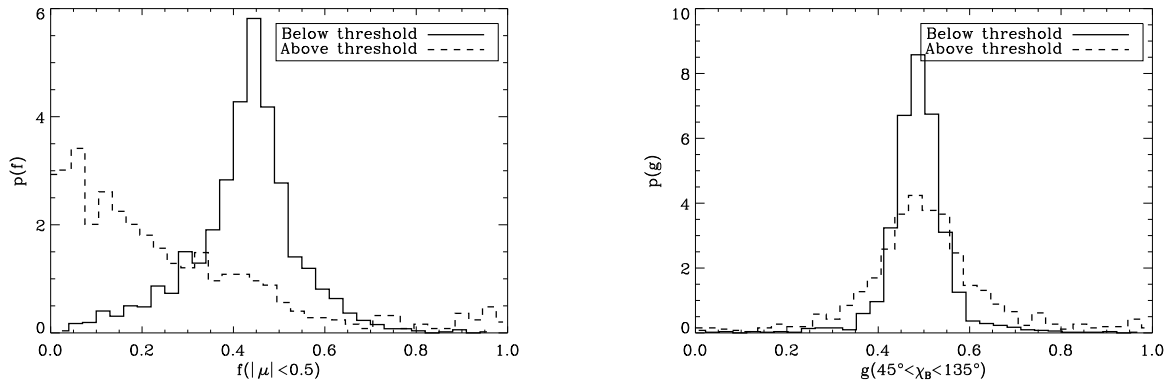


FIG. 9.— Histogram of the posterior distribution mass for the inclination normalized to the total area of the posterior (left panel) in different inclination regimes. The right panel shows the posterior distribution mass for the azimuth between 45° and 135° . The results suggest that the field is quasi-isotropic for those points whose polarimetric signal is below 4.5 times the noise level.

We thank L. Bellot Rubio, J. C. del Toro Iniesta, A. López Ariste, D. Orozco Suárez and J. Trujillo Bueno for fruitful discussions. Financial support by the Span-

ish Ministry of Education and Science through project AYA2007-63881 is gratefully acknowledged.

REFERENCES

- Asensio Ramos, A., Martínez González, M. J., López Ariste, A., Trujillo Bueno, J., & Collados, M. 2007a, *ApJ*, 659, 829
- Asensio Ramos, A., Martínez González, M. J., & Rubiño Martín, J. A. 2007b, *A&A*, 476, 959
- David, H. A. 1981, *Order Statistics*, 2nd ed. (New York: Wiley)
- Domínguez Cerdeña, I., Sánchez Almeida, J., & Kneer, F. 2003, *A&A*, 407, 741
- . 2006, *ApJ*, 646, 1421
- Gelman, A., Roberts, G. O., & Gilks, W. R. 1996, in *Bayesian Statistics 5*, ed. J. M. Bernardo, J. Berger, A. Dawid, & A. Smith, 599
- Gregory, P. C. 2005, *Bayesian Logical Data Analysis for the Physical Sciences* (Cambridge: Cambridge University Press)
- Khomenko, E. V., Collados, M., Solanki, S. K., Lagg, A., & Trujillo Bueno, J. 2003, *A&A*, 408, 1115
- Kosugi, T., Matsuzaki, K., Sakao, T., Shimizu, T., Sone, Y., Tachikawa, S., Hashimoto, T., Minesugi, K., Ohnishi, A., Yamada, T., Tsuneta, S., Hara, H., Ichimoto, K., Suematsu, Y., Shimojo, M., Watanabe, T., Shimada, S., Davis, J. M., Hill, L. D., Owens, J. K., Title, A. M., Culhane, J. L., Harra, L. K., Doschek, G. A., & Golub, L. 2007, *Sol. Phys.*, 243, 3
- Kullback, S., & Leibler, A. 1951, *Annals of Mathematical Statistics*, 22, 79
- Lin, H. 1995, *ApJ*, 446, 421
- Lin, H., & Rimmele, T. 1999, *ApJ*, 514, 448
- Lites, B. W., Elmore, D. F., Stander, K. V., Akin, D. L., Berger, T., Duncan, D. W., Edwards, C. G., Francis, B., Hoffmann, C., Katz, N., Levay, M., Mathur, D., Rosenberg, W. A., Sleight, E., Tarbell, T. D., Title, A. M., & Torgerson, D. 2001, in *Presented at the Society of Photo-Optical Instrumentation Engineers (SPIE) Conference*, Vol. 4498, *Proc. SPIE* Vol. 4498, p. 73-83, *UV/EUV and Visible Space Instrumentation for Astronomy and Solar Physics*, ed. O. H. Siegmund, S. Fineschi, & M. A. Gummin, 73
- Lites, B. W., Kubo, M., Socas-Navarro, H., Berger, T., Frank, Z., Shine, R., Tarbell, T., Title, A., Ichimoto, K., Katsukawa, Y., Tsuneta, S., Suematsu, Y., Shimizu, T., & Nagata, S. 2008, *ApJ*, 672, 1237
- Lites, B. W., & Socas-Navarro, H. 2004, *ApJ*, 613, L600
- López Ariste, A., Malherbe, J. M., Manso Sainz, R., Asensio Ramos, A., Ramírez Vélez, J. C., & Martínez González, M. 2007, in *SF2A-2007: Proceedings of the Annual meeting of the French Society of Astronomy and Astrophysics held in Grenoble, France, July 2-6, 2007*, Eds.: J. Bouvier, A. Chalabae, and C. Charbonnel, p.592, ed. J. Bouvier, A. Chalabae, & C. Charbonnel, 592
- López Ariste, A., Tomczyk, S., & Casini, R. 2002, *ApJ*, 580, 519
- . 2006, *A&A*, 454, 663
- Martínez González, M. J., Collados, M., & Ruiz Cobo, B. 2006a, *A&A*, 456, 1159
- Martínez González, M. J., Collados, M., & Ruiz Cobo, B. 2006b, in *ASP Conf. Ser.*, Vol. 358, *Solar Polarization 4*, ed. R. Casini & B. W. Lites, 36
- Martínez González, M. J., Asensio Ramos, A., López Ariste, A., & Manso Sainz, R. 2008a, *A&A*, 479, 229
- Martínez González, M. J., Collados, M., Ruiz Cobo, B., & Beck, C. 2008b, *A&A*, 477, 953
- Metropolis, N., Rosenbluth, A. W., Rosenbluth, M. N., Teller, A. H., & Teller, E. 1953, *J. Chem. Phys.*, 21, 1087
- Neal, R. M. 1993, *Probabilistic Inference Using Markov Chain Monte Carlo Methods* (Dept. of Statistics, University of Toronto: Technical Report No. 0506)
- Orozco Suárez, D., Bellot Rubio, L. R., & del Toro Iniesta, J. C. 2007a, *ApJ*, 662, L31
- Orozco Suárez, D., Bellot Rubio, L. R., Del Toro Iniesta, J. C., Tsuneta, S., Lites, B., Ichimoto, K., Katsukawa, Y., Nagata, S., Shimizu, T., Shine, R. A., Suematsu, Y., Tarbell, T. D., & Title, A. M. 2007b, *PASJ*, 59, 837
- Orozco Suárez, D., Bellot Rubio, L. R., del Toro Iniesta, J. C., Tsuneta, S., Lites, B. W., Ichimoto, K., Katsukawa, Y., Nagata, S., Shimizu, T., Shine, R. A., Suematsu, Y., Tarbell, T. D., & Title, A. M. 2007c, *ApJ*, 670, L61
- Orozco Suárez, D., & Del Toro Iniesta, J. C. 2007, *A&A*, 462, 1137
- Ramírez Vélez, J. C., & López Ariste, A. 2007, *Memorie della Societa Astronomica Italiana*, 78, 54
- Ramírez Vélez, J. C., López Ariste, A., & Semel, M. 2008, *A&A*, 487, 731
- Socas-Navarro, H., Martínez Pillet, V., & Lites, B. W. 2004, *ApJ*, 611, 1139
- Socas-Navarro, H., & Sánchez Almeida, J. 2002, *ApJ*, 565, 1323
- Stenflo, J. O. 1994, *Solar Magnetic Fields. Polarized Radiation Diagnostics* (Dordrecht: Kluwer Academic Publishers)
- Trujillo Bueno, J., Asensio Ramos, A., & Shchukina, N. 2006, in *ASP Conf. Ser.*, Vol. 358, *Solar Polarization 4*, ed. R. Casini & B. W. Lites, 269
- Trujillo Bueno, J., Shchukina, N., & Asensio Ramos, A. 2004, *Nature*, 430, 326
- Vögler, A., Shelyag, S., Schüssler, M., Cattaneo, F., Emonet, T., & Linde, T. 2005, *A&A*, 429, 335
- Westendorp Plaza, C., del Toro Iniesta, J. C., Ruiz Cobo, B., Martínez Pillet, V., Lites, B. W., & Skumanich, A. 1998, *ApJ*, 494, 453

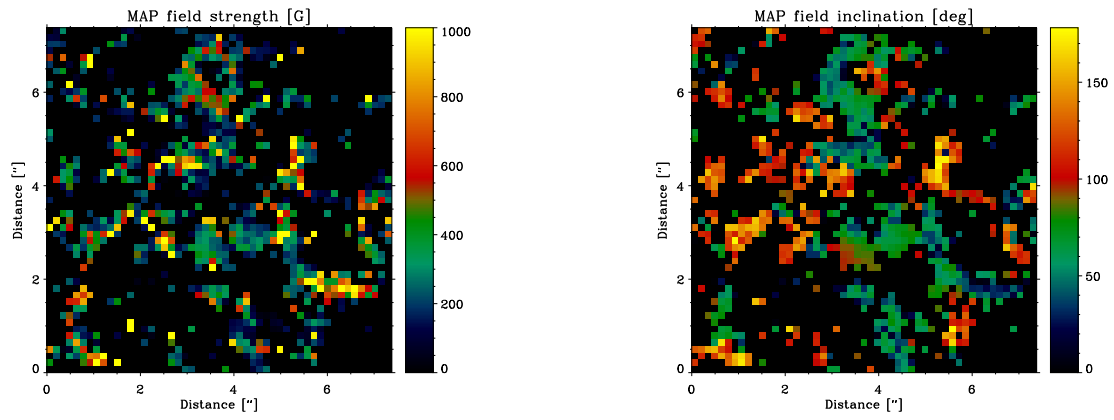


FIG. 10.— Maximum a-posteriori values for the field strength and the field inclination. These results agree well with those in Fig. 2 of Orozco Suárez et al. (2007c). Only the result for pixels with polarimetric signal above the threshold are shown.